

## Size effects on the mechanical properties of nanoporous graphene networks

*Dai-Ming Tang, Cui-Lan Ren, Ling Zhang\*, Ying Tao, Peng Zhang, Wei Lv, Xiang-Ling Jia, Xiaojuan Jiang, Guangmin Zhou, Takahito Ohmura, Ping Huai, Feng Li, Yoshio Bando, Dmitri Golberg\*, Quan-Hong Yang\**

Dr. D. Tang, Prof. T. Ohmura, Prof. Y. Bando, Prof. D. Golberg  
National Institute for Materials Science (NIMS), Namiki 1-1 and Sengen 1-2-1, Tsukuba, Ibaraki, 305-0044, Japan  
E-mail: GOLBERG.Dmitri@nims.go.jp

C.-L. Ren, Dr. P. Huai  
Shanghai Institute of Applied Physics, and Key Laboratory of Interfacial Physics and Technology, Chinese Academy of Sciences, Shanghai 201800, China

Prof. L. Zhang, X. Jiang,  
Electron Microscopy Center of Chongqing University, College of Materials Science and Engineering, Chongqing University, Shazhengjie 174, Chongqing 400044, China  
E-mail: zhangling2014@cqu.edu.cn

Dr. Y. Tao, X. Jia, Prof. Q.-H. Yang  
Nanoyang Group, State Key Laboratory of Chemical Engineering, School of Chemical Engineering and Technology, Tianjin University, and Collaborative Innovation Center of Chemical Science and Engineering, Tianjin, 300072, China  
E-mail: qhyangcn@tju.edu.cn

Dr. P. Zhang, Dr. G. Zhou, Prof. F. Li  
Shenyang National Laboratory for Materials Science, Institute of Metal Research, Chinese Academy of Sciences, Shenyang 110016, China

Dr. W. Lv  
Shenzhen Key Laboratory for Graphene-Based Materials, Engineering Laboratory for Functionalized Carbon Materials, Graduate School at Shenzhen, Tsinghua University, Shenzhen, 518055, China

Dr. P. Huai  
School of Physical Science and Technology, ShanghaiTech University, Shanghai 201210, China

Prof. Y. Bando  
Australian Institute for Innovative Materials, University of Wollongong, Squires Way, North Wollongong, NSW 2500, Australia

Prof. D. Golberg  
School of Physics, Chemistry and Mechanical Engineering, Queensland University of Technology (QUT), 2 George St., Brisbane, QLD 4000, Australia

Keywords: Graphene, three-dimensional assembly, mechanical properties, size effects, in situ electron microscopy, nanoindentation

**Abstract**

It is essential to understand the size scaling effects on the mechanical properties of graphene networks to realize the potential mechanical applications of graphene assemblies. Here, we use a “highly dense-yet-nanoporous graphene monolith (HPGM)” as a model material of graphene networks to investigate the dependence of mechanical properties on the intrinsic interplanar interactions and the extrinsic specimen size effects. The interactions between graphene sheets could be enhanced by heat treatment and the plastic HPGM is transformed into a highly elastic network. A strong size effect was revealed by in situ compression of micro- and nano-pillars inside electron microscopes. Both the modulus and strength are drastically increased as the specimen size reduces to  $\sim 100$  nm, because of the reduced weak links in a small volume. Molecular dynamics simulations reveal the deformation mechanism involving slip-stick sliding, bending, buckling of graphene sheets, collapsing and densification of graphene cells. In addition, a size-dependent brittle-to-ductile transition of the HPGM nanopillars is discovered and understood by the competition between volumetric deformation energy and critical dilation energy.

**1. Introduction**

Carbon nanomaterials are crucial for mechanical applications, such as MEMS and NEMS sensors and structural composite materials, because of the extremely strong carbon-carbon bonds, as demonstrated by the ultimately high stiffness and strength of individual  $sp^2$  bonded graphene,<sup>[1]</sup> carbon nanotubes,<sup>[2]</sup> and  $sp^3$  bonded diamond nanowires.<sup>[3]</sup> Over the last decade, various macro monoliths have been fabricated through assembling graphene and graphene oxide sheets,<sup>[4]</sup> in the form of papers,<sup>[5]</sup> fibers,<sup>[6]</sup> aerogels and foams,<sup>[7]</sup> and compact blocks.<sup>[8]</sup> Diverse mechanical properties and behaviors have been demonstrated. For example, near isotropic graphene monoliths have been constructed by densely packing graphene sheets, with

the compressive strength over 200 MPa.<sup>[5a, 8]</sup> Silicate-bridged graphene assembly (SGA) has a high hardness up to 13.1 GPa.<sup>[9]</sup> In addition, graphene fibers with the modulus  $\sim 280$  GPa and tensile strength  $\sim 1.45$  GPa have been reported.<sup>[10]</sup> In contrast, ultralight graphene foams with the pores larger than 10 micrometers demonstrated superelasticity with up to 90 % strain.<sup>[7a, 7c, 7f]</sup> A recent theoretical simulation on the three-dimensional graphene cellular assemblies predicted that their specific strength is potentially much higher than that of steel, at a relatively high density.<sup>[11]</sup> However, the fundamental questions of the deformation mechanism, intrinsic microstructure and extrinsic size effects have rarely been studied, particularly utilizing experimental approaches.

In this work, a “highly dense-yet-porous graphene monolith (HPGM)” is used as a model material to investigate the mechanical properties and behaviors of graphene networks, with a particular interest in the influences of intrinsic interplanar interactions and extrinsic specimen size, these questions have been extensively and intensively investigated for many other materials.<sup>[2-3, 12]</sup> The graphitic sheets are crumpled and entangled to form a three-dimensional nano-porous network, combining two seemingly incompatible properties: high porosity with a specific surface area  $\sim 370$  m<sup>2</sup>/g and a high density  $\sim 1.6$  g/cm<sup>3</sup>.<sup>[13]</sup> Such high-density porous carbon based materials have demonstrated superior performance in energy storage devices, such as supercapacitors with high volumetric capacitance<sup>[13-14]</sup>, Li-ion batteries,<sup>[15]</sup> and Li-S batteries with high volumetric energy density.<sup>[16]</sup> Here, the mechanical behaviors of HPGM are investigated at multiple length scales by nanoindentation and in situ compression inside a scanning electron microscope (SEM) and a transmission electron microscope (TEM). It is discovered that the rigidity of the graphene networks could be enhanced by heat treatments. High plasticity and high elasticity are obtained with the HPGM treated at room temperature and high temperatures, respectively. In addition, with the decrease of the specimen size, both the compressive strength and modulus are drastically increased, along with a brittle-to-ductile transition. Molecular dynamics (MD) simulations reveal the deformation mechanism including

sliding and bending of weakly linked graphene sheets, buckling and densification of strongly linked graphene sheets, followed by collapsing and densification of graphene cells. The size effects on the strength, modulus, and mechanical behaviors are explained in the frame of a network model considering weak and strong links and the competition of deformation energy and dilation energy.

## 2. Results and Discussion

X-ray tomography (Figure S1) shows the macroscopically uniform, isotropic and compact structure, consistent with the high packing density. TEM characterizations of HPGM treated at room temperature and high temperatures (HPGM-RT and HPGM-HT) are shown in Figure 1. During drying of the graphene hydrogel, capillary force induced the graphene sheet to be curved, crumpled, entangled and assembled around the evaporating and shrinking liquid template to form a nanoporous network, as depicted by the schematics (Figure 1a) and TEM image (Figure 1c). The cellular diameters are in the range of 3~5 nm, and the wall thicknesses are around 3 nm, i.e. a few graphitic layers. From the curved graphene fringes, the graphene sheets are assembled with random orientations. It is worth pointing out that the size of individual graphene sheets is about several micrometers, therefore it is reasonable to assume that they are in a highly crumpled state and extended to hundreds of nanometers and tens of cells. Because of the highly anisotropic structure of the graphene sheet with strong covalent bonding in plane and van der Waals forces between planes, the cellular boundaries within one continuous graphene sheet are expected to be strongly linked. And those pores composed of different graphene sheets are expected to have weak links. After heat treatment at 1600 °C, the nanoporous structure of HPGM-HT is well kept, and the atomic structure became more ordered, as depicted by the straight graphitic fringes (Figure 1b, d). It is also noted that rounded pores are changed into polyhedron-like shapes, also indicating the reconstruction of graphitic planes. Because of the enhancement of crystalline structure and interactions between the graphitic planes, the flexible

network of the HPGM-RT is transformed into a rigid network of the HPGM-HT.

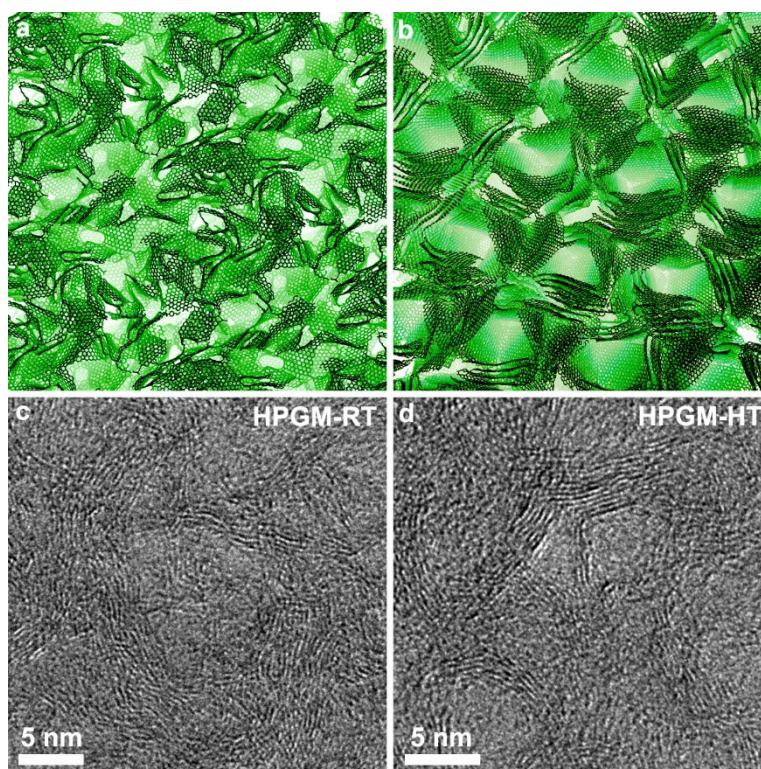


**Figure 1 Structure of nanoporous graphene networks.** (a, c) Schematic and TEM image of graphene assemblies, where curved graphene sheets are entangled into a three-dimensional nanoporous flexible network. (b, d) After heat-treatment at 1600 °C, the graphene fringes become straight, revealing enhanced crystallinity and interplanar interactions of a rigid network.

Nanoindentation was used to characterize the mechanical properties of the bulk HPGM treated at different temperatures (Figure S2). With a load limited to 5 mN, the indented depth for the HPGM-RT could reach up to ~1100 nm. The maximum depth reduced dramatically, to only ~542 nm for the HPGM-HT treated at 1600 °C, demonstrating an enhanced hardness. When the indenter was retracted, HPGM-RT and HPGM-HT unveiled distinct behaviors, with the HT treated samples elastically recovered to the initial position, while HPGM-RT showed a plastic deformation of ~37 %. Indeed, the extracted reduced modulus and nanohardness are both enhanced when the HPGM was heat treated. HPGM-RT is quite soft with the modulus and hardness averaged at ~2.95 GPa and ~0.20 GPa, respectively. In contrast, the modulus and hardness reached ~9.08 GPa and ~1.00 GPa for HPGM-HT. The different moduli imply changes

in the deformation mechanism, with the modulus of HPGM-RT close to  $C_{44}$  of graphite corresponding to sliding between graphitic layers,<sup>[17]</sup> and the modulus of HPGM-HT is close to that of isotropic graphite.<sup>[18]</sup> Nanoindentation experiments at different loading and depth have been conducted for both HPGM-RT and HPGM-HT (Figure S3). It is interesting to notice that both the modulus and hardness are decreased along with the increase of the penetrating depth and contact volume, indicating a size effect on the mechanical properties. The indentation process was observed by in situ SEM imaging, as demonstrated in Figure 2. The plastic deformation of HPGM-RT and elastic recovery of HPGM-HT are well captured by SEM images before and after indentation. While a triangular imprint was left on the surface of HPGM-RT under loading to 10 mN (Figure 2b), only a slight trace was detected after the indentation for HPGM-HT, even the load was 30 mN (Figure 2e). Under a load of 30 mN, the plastic deformation for the HPGM-RT was ~65 %. In contrast, HPGM-HT could recover elastically to ~92 % even under a load of 80 mN. The change in mechanical behaviors is consistent with the alteration of microstructures. After high temperature treatment, the interactions between graphene planes and, in turn, the crystalline order are enhanced, as revealed by the HRTEM image (Figure 1), and pronounced (002) peak from X-ray diffraction (XRD).<sup>[13]</sup> As a result of the enhanced rigidity, easy interplanar sliding is restricted, and HPGM was transformed from a flexible network with high plasticity to a highly elastic network.



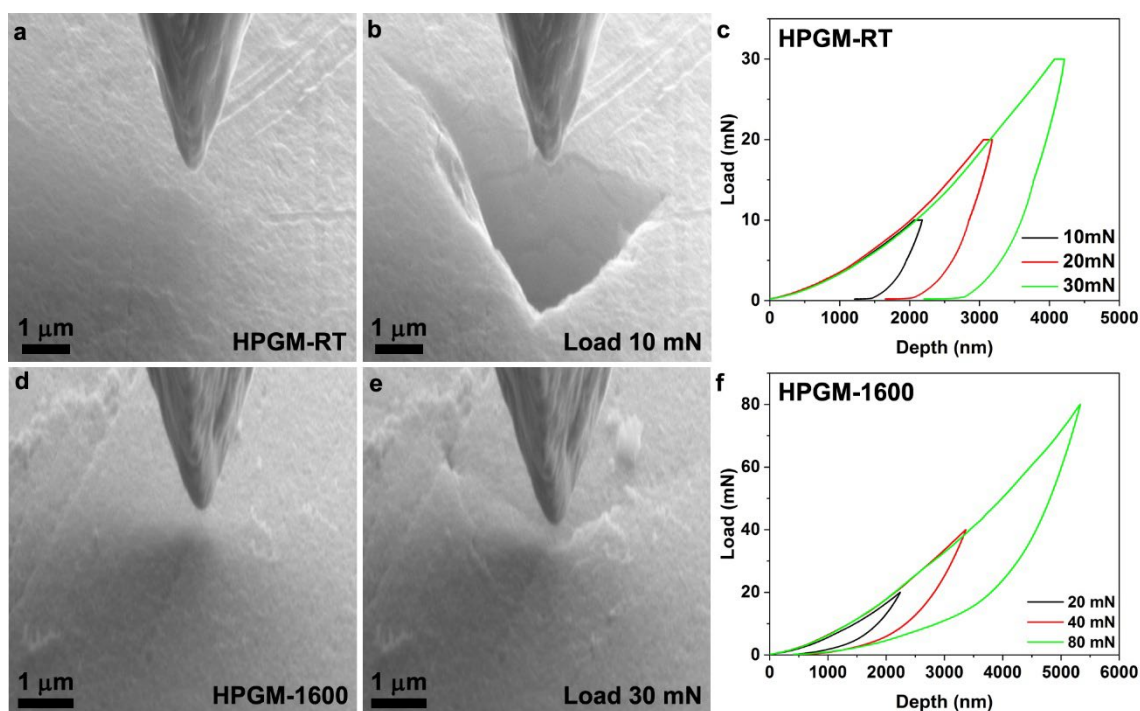


**Figure 2 Mechanical characterizations of bulk HPGM by in situ SEM nanoindentation.**

(a-b) SEM images of HPGM-RT before and after nanoindentation under a load of 10 mN. (c) Load-displacement curves of HPGM-RT with the loads limited at 10 mN, 20 mN and 30 mN, revealing a plastic deformation. (d-e) SEM images of HPGM-HT before and after nanoindentation under a load of 30 mN. (f) Load-displacement curves of HPGM-HT with the loads limited at 20 mN, 40 mN and 80 mN, characterized by the elastic recovery.

To investigate the size effects on the compressive properties of HPGMs, micro- and nano-pillars with a diameter ranging from  $\sim 100$  nanometers to  $\sim 5$  micrometers were fabricated by focused ion beam (FIB). SEM images of a HPGM-RT micropillar before and after compression are shown in Figure 3a-b and the stress-strain curve is depicted in Figure 3c. The pillar has a diameter of  $4.1 \mu\text{m}$  and a height of  $8.0 \mu\text{m}$ . Multiple yielding-cracking events were detected with the first yield at a stress of  $156.5 \text{ MPa}$  and a strain of  $8.6 \%$ . The pillar was continuously compressed revealing a stress plateau at  $\sim 205 \text{ MPa}$ , until the retraction of the indenter at a strain of  $58.0 \%$ . After unloading, a plastic deformation of  $40.9 \%$  was recorded, corresponding to  $\sim 70.5 \%$  of the maximum strain. SEM image after compression shows multiple cracks initialized from the top and side portions. An interesting waving morphology is observed as a

result of layer-by-layer buckling. Therefore, even though cracks were initiated and propagated, no catastrophic failure was observed, indicating that stress concentration at the crack tips could be effectively dissipated through the highly curved and interlinked flexible graphitic network. Repeated compression on the same HPGM micropillar has been conducted. A second loading demonstrated a similar linear relation in elastic region but showed a slightly higher modulus at a larger displacement (Figure S4) due to partial densification during the first loading. Then compression tests were carried out on the HPGM-HT micropillars (Figure S5). Compared with the HPGM-RT pillars, the modulus and maximum stress are both enhanced, consistent with the nanoindentation results. The ultimate failure is featured by a catastrophic stress drop at 0.45 GPa at a strain of  $\sim 8.8\%$ . The pillar was bounced off after the brittle fracture, as revealed by the SEM image in Figure S5b. The distinct mechanical properties of HPGM-RT and HPGM-HT are consistent with the mechanical behaviors revealed by nanoindentation, reflecting a flexible network for the former and a rigid network for the latter.

Smaller pillars of HPGM-RT with a diameter smaller than  $1\ \mu\text{m}$ , named as nanopillars, were compressed inside a TEM. Figure S6 and Figure S7 demonstrate the compression properties of two nanopillars, with the diameters of  $\sim 575\ \text{nm}$  and  $\sim 357\ \text{nm}$ , respectively. For both pillars, cracks were observed to nucleate and propagate from the top, representing a quasi-brittle behavior, like that of the micropillars. However, as the diameters decrease, the maximum stress, defined as the strength, was drastically enhanced, from  $\sim 0.21\ \text{GPa}$  (micropillars) to  $\sim 0.91\ \text{GPa}$  and  $\sim 1.57\ \text{GPa}$  (nanopillars). Such a “smaller, stronger” trend is revealed for the first time for the graphene assemblies and is consistent with the discovery of the ultra-strength materials with nanoscale structural features.<sup>[19]</sup>

HPGM-RT nanopillars with diameters around  $300\ \text{nm}$  were further tested under compression, as demonstrated in Figure 3d-f and Figure S8. Instead of cracking, only plastic yielding was observed. A high magnification TEM image of the severely deformed area (Figure 3f) reveals a collapsed cellular structure. Such an observation is consistent with the classical deformation



mechanism of cellular materials, starting from bending and buckling of the walls followed by densification due to collapse of cells.<sup>[20]</sup> For even smaller nanopillars with diameters around 100 nm, it was difficult to avoid bending during compression, due to a possible slight asymmetry of the testing configuration or the non-uniform deformation process due to inhomogeneous cellular structure at nanometer scale. Under bending, one side experiences a compressive stress, and the other side is under tensile stress. As revealed in Figure S9, even though the nanopillar was bent to  $\sim 92.4^\circ$ , no crack was observed, demonstrating an enhanced ductility as the size reducing from micrometer to nanometer scales. Typical stress-strain curves of HPGM-RT nanopillars with different diameters are presented in Figure 3g. For the relatively large pillars, multiple yielding-cracking was observed at a relatively low stress level. For the smaller pillars, the yielding stress was enhanced to  $\geq 1$  GPa, while the yielding strain was compromised. The size effects on the mechanical properties are summarized in Figure 3h-i. Apparently, as the diameters are reduced from  $\sim 1$   $\mu\text{m}$  to  $\sim 200$  nm, both modulus and strength are greatly enhanced. In the meantime, it is noticed that the scattering of the data points also increases, reflecting the variation of the specific local structure in a small volume. It is worth pointing out that the moduli of the nanopillars could be as high as  $\sim 33$  GPa, close to  $C_{33}$  of graphite crystals,<sup>[21]</sup> corresponding to the compression between the graphitic layers, indicating that the interlayer sliding mode is restricted in the nanoscale HPGM.

The mechanical properties of the HPGM are compared with typical carbon materials, as plotted in Figure 3j. Because of the strong carbon-carbon bonds, the intrinsic strength of both  $\text{sp}^3$  bonded diamond and  $\text{sp}^2$  bonded graphene are extremely high, as represented by the near 100 GPa strength of individual diamond nanowires,<sup>[3]</sup> graphene monolayers,<sup>[1a-c, 22]</sup> graphene oxide sheets,<sup>[1d, 23]</sup> and carbon nanotubes.<sup>[2, 24]</sup> Besides the individual nanostructures, various kinds of three dimensional graphene monoliths have been fabricated, with the mechanical properties largely scaling with the packing density.<sup>[11]</sup> For example, compact graphene monolith demonstrates quite high strength  $\sim$  hundreds of MPa.<sup>[8, 25]</sup> Well aligned graphene papers and

fibers could have tensile strength  $> 1$  GPa.<sup>[5a, 5c, 6b, 6d-f]</sup> In the meantime, ultra-elasticity up to  $\sim 90\%$  of recovery has been shown by the light-weight graphene aerogels.<sup>[7b, 7c, 7f]</sup> Compared with generally brittle conventional graphite based materials with a typical strength limited to  $\sim 100$  MPa,<sup>[21]</sup> carbon nanomaterials have superior mechanical properties. The mechanical properties of bulk HPGM-RT in the current work, such as modulus, hardness, and strength, are close to the compactly packed graphene monoliths, consistent with the general density-dominated scaling law. However, a strong size effect is discovered for the HPGM nanopillars, with a remarkable combination of a high strength, up to  $\sim 1.7$  GPa, and a ductility of  $\sim 15\%$ .

The mechanical properties and size effects of HPGM could be understood via analyzing a network model including weak and strong links (Figure 4a). Micrometer scale graphene sheets are stacked and assembled into a nanoporous structure. The crystalline order determines the interaction between the graphene planes and the network rigidity. The interactions between the graphene sheets could be tuned by heat treatment, as a result, the modulus of HPGM-HT is notably enhanced compared with that of HPGM-RT. In addition, there are two types of links connecting the cells. If the neighboring cells are connected by an extended graphene sheet, a strong link of covalent bonding is expected. Otherwise, only a weak link of van der Waals forces exists. The number of weak links is proportional to the sample volume. The reduced weak links could explain the enhanced strength of the HPGM nanopillars. In addition, it is reasonable to assume that the deformation mechanisms of the weak and strong links are different, with easy sliding for the former and more resistant compression for the latter. As a result, the modulus is enhanced from  $\sim 5$  GPa (interplanar sliding mode of  $C_{44}$ ) to  $\sim 33$  GPa (interplanar compression mode of  $C_{33}$ ).

The size dependent mechanical behaviors of HPGM-RT pillars could be further analytically understood by considering the competition between two behaviors under compression, namely, plastic buckling of the cellular structures due to compressive stress and dilation due to transverse strains. The two mechanisms compete and the dominating one determines the overall

mechanical behavior. Split cracking will occur when the volumetric deformation energy ( $U_V$ ) is larger than the critical dilation energy ( $W_V$ ). The volumetric deformation energy<sup>[1b]</sup> and critical dilation energy<sup>[26]</sup> could be expressed as:  $U_V = \frac{(1-2\nu)\sigma^2}{6E}$  (1), and  $W_V = \frac{K\chi_c^2}{2}$  (2), where  $\nu$  is Poisson's ratio,  $\sigma$  is the normal stress,  $E$ ,  $K$  are Young's modulus and bulk modulus, and  $\chi_c$  is the critical volumetric strain. According to the experimental results, there is a critical cracking strain ( $\varepsilon_c$ ). The related critical volumetric strain ( $\chi_c$ ) can be calculated by the following equation:  $\chi_c \approx (1 - 2\nu)\varepsilon_c$  (3). The relationship between elastic modulus and Poisson's ratio is:  $E = 3K(1 - 2\nu)$  (4). Considering the condition required for split cracking,  $U_V > W_V$ , and Eqs. (1-4), when the applied stress reached the plastic instability strength, the critical elastic modulus for split cracking ( $E_c$ ) can be obtained:  $E_c = \frac{\sigma_{pi}}{\varepsilon_c}$  (5), where  $\sigma_{pi}$  is the size dependent strength and  $\varepsilon_c$  is the critical strain for initialize a crack. If the specimen size is smaller than this critical value, with  $E > E_c$ , the plastic instability would preferentially occur. On the opposite, split cracking will be initiated when the specimen size is larger than the critical size, with  $E < E_c$ .

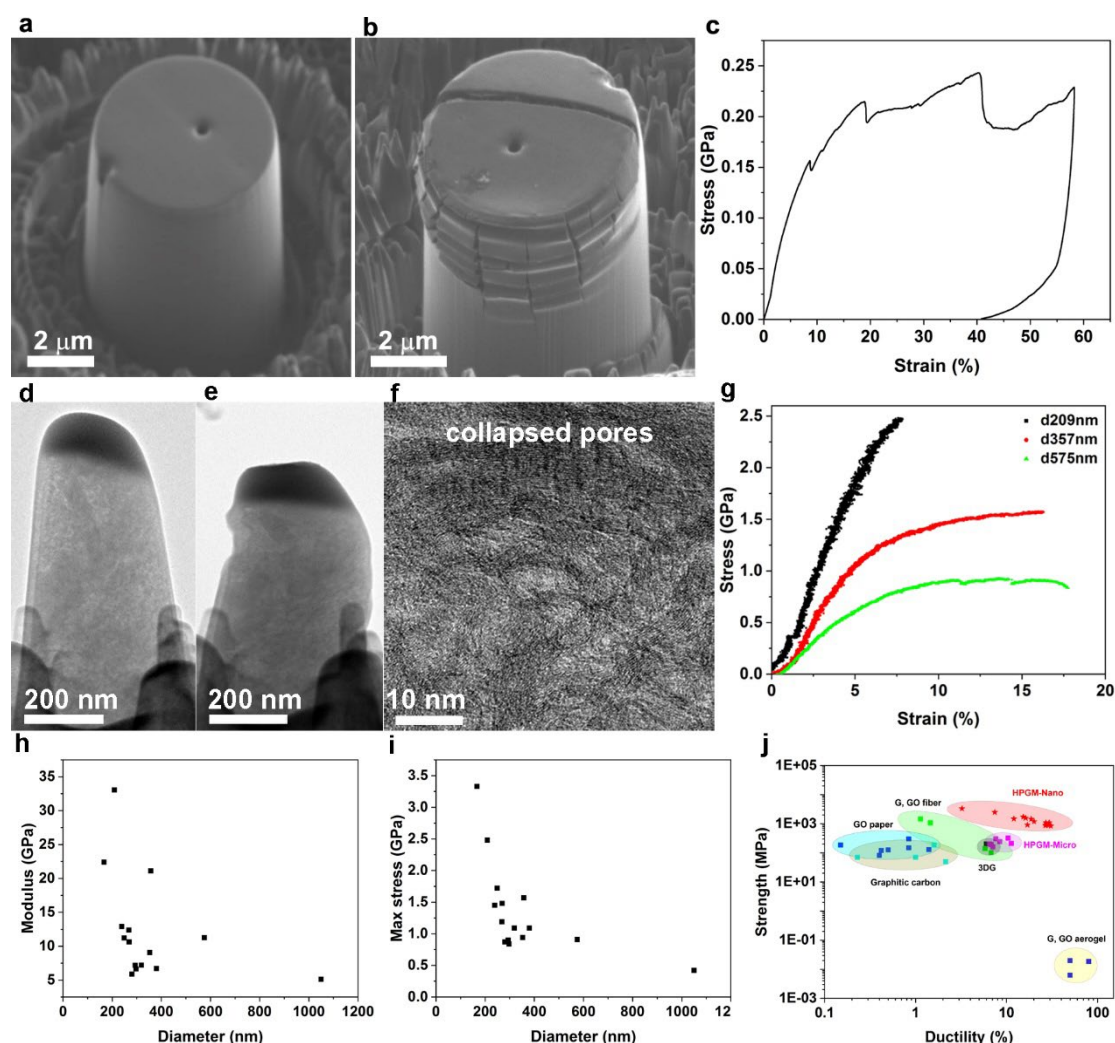


**Figure 3 Mechanical properties of HPGM micro- and nano-pillars** (a-b) SEM images before and after a compression test on a HPGM-RT micropillar. The side surface shows a periodic buckling feature, with multiple cracks detected both at the top and side portions. (c) Stress-strain curve revealing multiple yielding-cracking events. (d-e) TEM images before and after a compression test on a HPGM-RT nanopillar. The pillar was plastically deformed and the side surface shows a waving feature. (f) High magnification TEM image of a severely deformed area, unveiling the collapsed porous structure. (g) Typical stress-strain curves until yielding of HPGM nanopillars with different diameters. (h-i) Dependence of modulus and maximum stress on the pillar diameter, demonstrating a clear “smaller, harder and stronger” trend. (j) Strength versus ductility of the HPGM micro- and nano-pillars, compared with typical carbon materials (Table S1).

Molecular dynamics (MD) simulations have been carried out to understand the atomic deformation mechanism of HPGM. Based on the structural model in Figure 4a, an ideal model of orderly packed graphene assembly was constructed to uncover the deformation mechanism (Figure S10a-e). In addition, randomly packed graphene assembly, closely modelling the experimental structure, was built to get an insight into the deformation processes (Figure S10f-h). The compression process of an orderly packed unit is featured by sequential sliding, bending, buckling and densification as the compressive stress and strain are increased (Figure S11). Along with the buckling of the graphene sheets, multiple abrupt stress drops were captured (Figure S11e). A  $2\times 2$  extended ordered graphene assembly is constructed by stacking the cubic units in three dimensions (Figure 4c). Strong and weak links are marked, for the joints with continuous and non-continuous graphene sheets. Under compression, sliding-bending was observed for the weakly linked graphene sheets, and buckling was observed for the strongly linked sheets. Densification was observed when the cellular structure was collapsed, along with the dramatic increase of slope in the stress-strain curve (Figure 4b). The essential size effect on the modulus of graphene assembly is well demonstrated by comparing the compression of the unit cell and the extended model. The slopes of stress-strain curves at around 10 % strain are calculated to be 16.3 GPa and 8.7 GPa, respectively, for the former and latter models. Because of the increased number of cells and weak links, the deformation of the extended model is not uniform. “Soft” cells connected with weak links tend to be compressed preferably, resulted in a lower modulus. With the specimen size approaching the critical size of crumpled single graphene sheets, there are no weak links and the interlayer sliding mode is restricted, well consistent with the experimentally measured modulus of near 33 GPa for the HPGM nanopillars with the diameter around 200 nm (Figure 3h). Randomly packed graphene assemblies with different densities have been modeled and tested in compression (Figure 4b,d). Distinct from the abrupt stress drops corresponding to the buckling events for the orderly packed model, the stress-strain curves of the randomly packed models are generally smoother, reflecting the

random orientation and isotropic structure. A higher stress was observed for the higher density models, reflecting the density scaled modulus. The atomic deformation mechanism is like that of the orderly packed models, including the sliding-bending of the loosely linked graphene sheets, buckling of the strongly linked sheets and final densification of the collapsed cells, also well consistent with the TEM observations (Figure 3f). The slope of the stress-strain curve is dependent on the compressive strain along with the change of deformation mode. Taking the model with density  $\sim 1.01 \text{ g/cm}^3$  as an example, the slopes at around 10 %, 20 %, 30 % and 40 % were documented to be  $\sim 9.0$ ,  $\sim 16.1$ ,  $\sim 21.0$ , and  $\sim 33.3 \text{ GPa}$ , reflecting the transition of deformation mechanism from sliding to compression. Because of the limited calculation capabilities, both the cell thickness ( $t$ ) and cell size ( $l$ ) are smaller than those of the HPGM structure. For cellular materials, both the relative density and modulus scale with the ratio of cell thickness to the cell size ( $t/l$ ).<sup>[20a]</sup> In addition, the bending strain is inversely proportional to the radius of the cell. Thus, smaller cells have higher rigidity. Such structural differences are reflected by the higher modulus from the MD simulations compared with the experimentally measured results.

A general “smaller, stronger and tougher” trend has been reported in many materials types, including crystalline metals<sup>[27]</sup>, metallic glasses<sup>[28]</sup>, semiconductor crystals<sup>[29]</sup>, ceramics composites<sup>[30]</sup> and even bones<sup>[31]</sup>. Many quasi-brittle materials demonstrate ductile behaviours when the specimen sizes are in the sub-micron region. Different types of materials demonstrate a similar size-scaling behaviour indicates there is a similar mechanism. Generally, brittle behaviours involve localized events such as the propagation of shear bands or cracks, which is size dependent following a Griffith-like criterion. In our work, the weak links in the graphene networks could be considered as micro-cracks. As the size decreases, the required stress for propagating cracks increases, until reaching a level to activate the buckling of the cells, leading to the brittle-to-ductile transition. Currently, the mechanical performance of HPGM at larger and bulk scales is limited by the weak links in the larger volume. Therefore, the key for practical



mechanical applications is to control the number and distribution of weak links. Possible strategies include transforming the weak van der Waals forces into strong covalent bonding by high temperature heat treatment, and introducing hetero ions or functional groups as bridges between graphitic sheets to fabricate graphene enhanced composite.

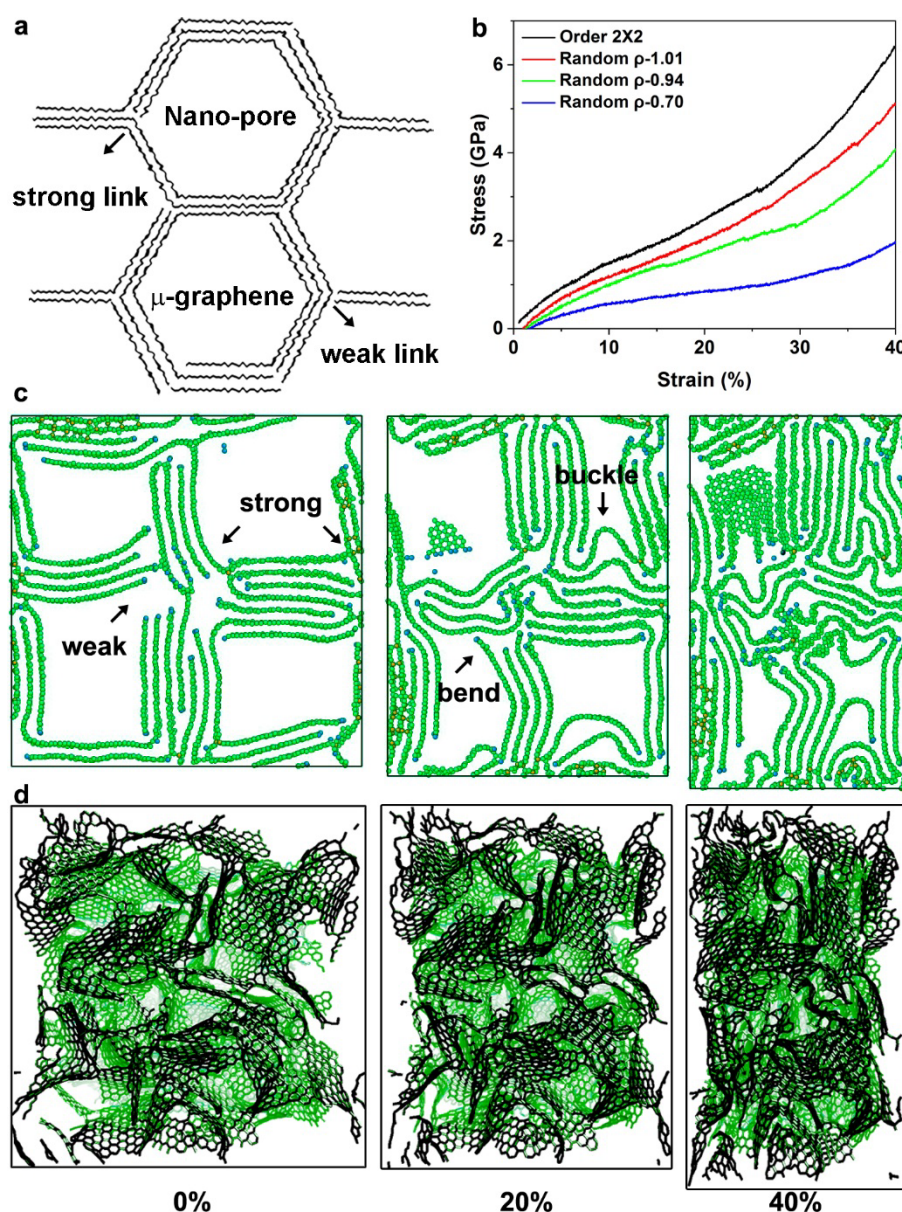


**Figure 4 Molecular dynamics simulation of deformation mechanism.** (a) Structural model of a nanoporous graphene network. Graphene sheets with micrometer dimensions are entangled into a nanoporous network, connected by weak and strong links. (b) Calculated stress-strain curves of ordered and random models with different packing densities. (c) Simulated compression process of an ordered graphene cellular structure, revealing the sliding-bending

mechanism at the weak links and buckling mechanism at the strong links. (d) Simulated compression process of random graphene porous structure. Stick-slip, bending, buckling, and densification could be identified depending on the local structure and stress level.

### 3. Conclusion

In summary, the mechanical properties of nanoporous graphene networks are investigated at multiple length scales by nanoindentation and in situ SEM and TEM compression, with an emphasis on the effects of intrinsic structural and extrinsic specimen size. It is revealed that intrinsic interplanar interactions and rigidity of the network could be enhanced by a high temperature heat treatment, resulted in a transition from high-plasticity to high-elasticity. With the specimen size decreasing from a micrometer to nanometer scale, because of the reduction of weak links in the network, both the modulus and strength are dramatically enhanced along with a brittle-to-ductile transition. Molecular dynamics simulations unveil the sliding, bending, buckling, collapsing and densification mechanisms. Because of the size strengthening effects, a remarkable combination of compressive strength  $\sim 1.7$  GPa and yielding strain  $\sim 15$  % is achieved for the nanoporous graphene nanopillars. The size effects revealed in this work bridges the gap between individual graphene sheets and carbon macro-monoliths, and are valuable for designing graphene-based materials and devices at multiple length scales.

### 4. Experimental Section

*Preparation and characterization of HPGM.* HPGM was fabricated by the method as previously reported.<sup>[13]</sup> Briefly, a GO colloidal suspension (2 mg/mL, 425 mL) made using modified Hummers method was sealed in a 500 mL Teflon-lined autoclave. Then it was moved to a muffle furnace for a hydrothermal process at 150 °C for 6 h. After the autoclave was cooled, the obtained black cylindrical hydrogel was washed with distilled water and then dried at room temperature. HPGM-HT was obtained by heat treatment at 1600 °C for 1 h. X-ray tomography

was conducted at a Versa XRM-500 desktop system (Xradia Inc.). The microstructure was characterized by a high-resolution transmission electron microscope (JEM-3100FEF), equipped with an OMEGA-type energy filter.

*Nanoindentation.* The specimen surfaces for nanoindentation were mechanically polished with a Silicon carbide P4000 grinding paper, and subsequently polished with a microcloth (Buehler) with water spray. The average roughness is smaller than 3 nm. Nanoindentation measurements were carried out using a Hysitron, Inc. Triboindenter with a Berkovich indenter. The tip truncation of the indenter was calibrated using fused silica. The Oliver and Pharr method was used for the tip calibration and the calculation of nanohardness.<sup>[32]</sup> The reduced modulus  $E_r$  was calculated by an analysis of the unloading curve and is expressed as  $E_r^{-1} = \frac{1-\nu_s^2}{E_s} + \frac{1-\nu_i^2}{E_i}$ , where  $E_s$  and  $\nu_s$  are the Young's modulus and the Poisson's ratio of the specimen, and  $E_i$  and  $\nu_i$  are the same parameters for the indenter. The loading and unloading rates of the indenter were 100  $\mu\text{N/s}$  for 1 mN, 5 mN, 9 mN and 14 mN peak loads. The probing sites and the indent configurations on the specimen surfaces were checked in situ with the SPM before and after the indentation measurements.

*Fabrication of micro- and nano-pillars.* Mechanically polished sample was used to fabricate nano- and micro-meter size pillars via focused ion beam (FIB, JEOL JIB-4000 or Zeiss Auriga dual beam FIB). For in situ tests in TEM, HPGM slices were glued to half-circled TEM grids and then subjected to FIB milling. Before milling, the sample surface was deposited with a carbon layer of about 400 nm in thickness to protect it from  $\text{Ga}^+$  irradiation. The pillars were milled under an acceleration voltage of 30 kV and a final current of 23 pA (JIB-4000 FIB) or 10 pA (JEM-9320 FIB) to reduce damage. For in situ tests in SEM, micro-pillars were milled out directly on the polished bulk sample with a final current of 120 pA.

*In situ indentation and compression inside SEM.* In situ nanoindentation and compression tests in SEM (Zeiss Auriga) were carried out using a PI 88 PicoIndenter (Hysitron Inc.) with a

cube corner indenter and a flat indenter (20  $\mu\text{m}$  in diameter), respectively. The stage was tilted for  $15^\circ$  to view the real time image. Displacement-controlled mode was applied with loading rates of 1-5  $\mu\text{m/s}$  for indentations and 5  $\text{nm/s}$  for micropillar compression. Repeated compression tests have been carried out to investigate possible non-linear or hysteresis behaviors. As shown in Figure S4, the loading-depth curves of a first and second test are largely overlapped at small strain region, demonstrating a linear relation. However, at larger displacement, a second loading demonstrated a higher force, indicating an enhanced modulus, probably due to partial densification during the first loading.

*In situ compression in TEM.* In situ compression measurements were carried out in a JEM-2010F TEM by using a PI 95 PicoIndenter (Hysitron Inc.). Flat indenter of 2.6  $\mu\text{m}$  in diameter was used. Displacement-controlled mode was applied with a loading rate of 2  $\text{nm/s}$ . During the mechanical measurements, the structural evolution of the HPGM pillars was monitored in real-time and recorded by a charge-coupled device (CCD). Possible deformation and displacement of the substrate during compression tests have been considered for correctly calculating the deformation of the micro- and nano-pillars.<sup>[33]</sup>

*Molecular dynamics simulations.* The compression properties were investigated by molecular dynamics (MD) simulations utilizing the LAMMPS package.<sup>[34]</sup> The interactions between carbon atoms were simulated by the adaptive intermolecular reactive empirical bond order (AIREBO) potential.<sup>[35]</sup> The interaction between graphene sheets and the fictitious balls were modeled with L-J potential with parameter  $\epsilon = 0.01 \text{ eV}$  and  $\sigma = 3.9 \text{ \AA}$  to obtain the models with different density. Such method was successfully used in a previous work to investigate the mechanics of a lightweight three-dimensional graphene assembly.<sup>[11]</sup> Newton's equation of motion was integrated using a Velocity Verlet algorithm. A fixed time step of 0.5 fs was used during the structural optimization and compression processes. The MD results were processed by the ATOMEYE package.<sup>[36]</sup> In order to quantify the deformation processes and to view the

defect evolution on the models, the atom colors were assigned according to their local coordination numbers.

### Supporting Information

Supporting Information is available from the Wiley Online Library or from the author.

### Acknowledgements

D.T. and C.R. contributed equally to this work. This work was supported from JSPS KAKENHI (25820336), National Natural Science Foundation of China (51522210) and State Key Research and Development Program of MOST of China (2016YFB0700403), Hundred Talents Program of CAS, International Center for Young Scientists (ICYS), World Premier International (WPI) Center for Materials Nanoarchitectonics (MANA), and TEM station of the National Institute for Materials Science (NIMS). Q.-H. Yang thanks the support from National Science Fund for Distinguished Young Scholars, China (No. 51525204). D. Golberg is grateful to the Australian Research Council (ARC) for granting an Australian Laureate Fellowship (FL 160100089). C.-L. Ren and P. Huai thank the support from Shanghai Municipal Science and Technology Commission (16ZR1443100) and Shanghai Supercomputer Center.

Received: ((will be filled in by the editorial staff))

Revised: ((will be filled in by the editorial staff))

Published online: ((will be filled in by the editorial staff))

### Conflict of interest

The authors declare no conflict of interest.

### References

- [1] a) C. Lee, X. Wei, J. W. Kysar, J. Hone, *Science* **2008**, *321*, 385; b) G.-H. Lee, R. C. Cooper, S. J. An, S. Lee, A. van der Zande, N. Petrone, A. G. Hammerberg, C. Lee, B. Crawford, W. Oliver, J. W. Kysar, J. Hone, *Science* **2013**, *340*, 1073; c) R. Grantab, V. B. Shenoy, R. S. Ruoff, *Science* **2010**, *330*, 946; d) J. W. Suk, R. D. Piner, J. An, R. S. Ruoff, *ACS Nano* **2010**, *4*, 6557.  
[2] a) M.-F. Yu, O. Lourie, M. J. Dyer, K. Moloni, T. F. Kelly, R. S. Ruoff, *Science* **2000**, *287*,



- 637; b) B. Peng, M. Locascio, P. Zapol, S. Li, S. L. Mielke, G. C. Schatz, H. D. Espinosa, *Nat. Nanotech.* **2008**, *3*, 626; c) M.-S. Wang, D. Golberg, Y. Bando, *Adv. Mater.* **2010**, *22*, 4071.
- [3] A. Banerjee, D. Bernoulli, H. Zhang, M.-F. Yuen, J. Liu, J. Dong, F. Ding, J. Lu, M. Dao, W. Zhang, Y. Lu, S. Suresh, *Science* **2018**, *360*, 300.
- [4] a) O. C. Compton, S. T. Nguyen, *Small* **2010**, *6*, 711; b) H.-P. Cong, J.-F. Chen, S.-H. Yu, *Chem. Soc. Rev.* **2014**, *43*, 7295; c) L. Qiu, Z. He, D. Li, *Adv. Mater.* **2018**, *30*, 1704850; d) L. Qiu, D. Li, H.-M. Cheng, *ACS Nano* **2018**, *12*, 5085; e) Y. Zhu, S. Murali, W. Cai, X. Li, J. W. Suk, J. R. Potts, R. S. Ruoff, *Adv. Mater.* **2010**, *22*, 3906.
- [5] a) D. A. Dikin, S. Stankovich, E. J. Zimney, R. D. Piner, G. H. B. Dommett, G. Evmenenko, S. T. Nguyen, R. S. Ruoff, *Nature* **2007**, *448*, 457; b) Z. Tang, S. Shen, J. Zhuang, X. Wang, *Angew. Chem. Int. Edit.* **2010**, *49*, 4603; c) D. Li, M. B. Muller, S. Gilje, R. B. Kaner, G. G. Wallace, *Nat. Nanotech.* **2008**, *3*, 101; d) S. Park, K.-S. Lee, G. Bozoklu, W. Cai, S. T. Nguyen, R. S. Ruoff, *ACS Nano* **2008**, *2*, 572; e) Z. An, O. C. Compton, K. W. Putz, L. C. Brinson, S. T. Nguyen, *Adv. Mater.* **2011**, *23*, 3842; f) H. Chen, M. B. Müller, K. J. Gilmore, G. G. Wallace, D. Li, *Adv. Mater.* **2008**, *20*, 3557; g) A. Eckert, T. Rudolph, J. Guo, T. Mang, A. Walther, *Adv. Mater.* **2018**, *30*, 1802477.
- [6] a) R. Cruz-Silva, A. Morelos-Gomez, H.-i. Kim, H.-k. Jang, F. Tristan, S. Vega-Diaz, L. P. Rajukumar, A. L. Elías, N. Perea-Lopez, J. Suhr, M. Endo, M. Terrones, *ACS Nano* **2014**, *8*, 5959; b) F. Meng, W. Lu, Q. Li, J.-H. Byun, Y. Oh, T.-W. Chou, *Adv. Mater.* **2015**, *27*, 5113; c) R. J. T. Nicholl, H. J. Conley, N. V. Lavrik, I. Vlassioulak, Y. S. Puzyrev, V. P. Sreenivas, S. T. Pantelides, K. I. Bolotin, *Nat. Commun.* **2015**, *6*, 8789; d) G. Xin, T. Yao, H. Sun, S. M. Scott, D. Shao, G. Wang, J. Lian, *Science* **2015**, *349*, 1083; e) Z. Xu, C. Gao, *Nat. Commun.* **2011**, *2*, 571; f) Z. Xu, C. Gao, *Accounts. Chem. Res.* **2014**, *47*, 1267; g) C. Zhu, T. Y.-J. Han, E. B. Duoss, A. M. Golobic, J. D. Kuntz, C. M. Spadaccini, M. A. Worsley, *Nat. Commun.* **2015**, *6*, 6962; h) Y. Zhang, J. Peng, M. Li, E. Saiz, S. E. Wolf, Q. Cheng, *ACS Nano* **2018**, *12*, 8901.
- [7] a) H. Hu, Z. Zhao, W. Wan, Y. Gogotsi, J. Qiu, *Adv. Mater.* **2013**, *25*, 2219; b) Z. Chen, W. Ren, L. Gao, B. Liu, S. Pei, H.-M. Cheng, *Nat. Mater.* **2011**, *10*, 424; c) S. Vinod, C. S. Tiwary, P. A. da Silva Autreto, J. Taha-Tijerina, S. Ozden, A. C. Chipara, R. Vajtai, D. S. Galvao, T. N. Narayanan, P. M. Ajayan, *Nat. Commun.* **2014**, *5*, 4541; d) H. Sun, Z. Xu, C. Gao, *Adv. Mater.* **2013**, *25*, 2554; e) Y. Xu, K. Sheng, C. Li, G. Shi, *ACS Nano* **2010**, *4*, 4324; f) L. Qiu, J. Z. Liu, S. L. Y. Chang, Y. Wu, D. Li, *Nat. Commun.* **2012**, *3*, 1241.
- [8] a) H. Bi, K. Yin, X. Xie, Y. Zhou, N. Wan, F. Xu, F. Banhart, L. Sun, R. S. Ruoff, *Adv. Mater.* **2012**, *24*, 5124; b) M. A. Worsley, S. Charnvanichborikarn, E. Montalvo, S. J. Shin, E. D. Tylski, J. P. Lewicki, A. J. Nelson, J. H. Satcher, J. Biener, T. F. Baumann, S. O. Kucheyev, *Adv. Funct. Mater.* **2014**, *24*, 4259.
- [9] H. Jin, Y. Bu, J. Li, J. Liu, X. Fen, L. Dai, J. Wang, J. Lu, S. Wang, *Adv. Mater.* **2018**, *30*, 1707424.
- [10] Z. Xu, Y. Liu, X. Zhao, L. Peng, H. Sun, Y. Xu, X. Ren, C. Jin, P. Xu, M. Wang, C. Gao, *Adv. Mater.* **2016**, *28*, 6449.
- [11] Z. Qin, G. S. Jung, M. J. Kang, M. J. Buehler, *Sci. Adv.* **2017**, *3*, e1601536.
- [12] a) Z. W. Shan, R. K. Mishra, S. A. S. Asif, O. L. Warren, A. M. Minor, *Nat. Mater.* **2008**, *7*, 115; b) D. Golberg, P. M. F. J. Costa, M.-S. Wang, X. Wei, D.-M. Tang, Z. Xu, Y. Huang, U. K. Gautam, B. Liu, H. Zeng, N. Kawamoto, C. Zhi, M. Mitome, Y. Bando, *Adv. Mater.* **2012**, *24*, 177.
- [13] Y. Tao, X. Xie, W. Lv, D. M. Tang, D. Kong, Z. Huang, H. Nishihara, T. Ishii, B. Li, D. Golberg, F. Kang, T. Kyotani, Q. H. Yang, *Sci. Rep.* **2013**, *3*, 2975.
- [14] a) Y. Xu, Y. Tao, X. Zheng, H. Ma, J. Luo, F. Kang, Q.-H. Yang, *Adv. Mater.* **2015**, *27*, 8082; b) X. Dong, H. Jin, R. Wang, J. Zhang, X. Feng, C. Yan, S. Chen, S. Wang, J. Wang, J. Lu, *Adv. Energy Mater.* **2018**, *8*, 1702695; c) H. Jin, J. Li, Y. Yuan, J. Wang, J. Lu, S. Wang, *Adv. Energy Mater.* **2018**, *8*, 1801007; d) J. Zhou, L. Hou, J. Lian, W. Cheng, D. Wang, H. Gou, F. Gao, *J. Mater. Chem. A* **2019**, *7*, 476; e) H. Jin, X. Feng, J. Li, M. Li, Y. Xia, Y. Yuan, C.

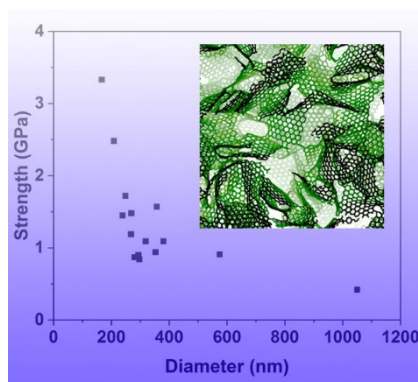


- Yang, B. Dai, Z. Lin, J. Wang, S. Wang, J. Lu, *Angew. Chem. Int. Edit.* **2019**, 0.
- [15] X. Wang, L. Lv, Z. Cheng, J. Gao, L. Dong, C. Hu, L. Qu, *Adv. Energy Mater.* **2016**, 6, 1502100.
- [16] a) Q. Pang, X. Liang, C. Y. Kwok, J. Kulisch, L. F. Nazar, *Adv. Energy Mater.* **2017**, 7, 1601630; b) H. Li, Y. Tao, C. Zhang, D. Liu, J. Luo, W. Fan, Y. Xu, Y. Li, C. You, Z.-Z. Pan, M. Ye, Z. Chen, Z. Dong, D.-W. Wang, F. Kang, J. Lu, Q.-H. Yang, *Adv. Energy Mater.* **2018**, 8, 1703438; c) C. Zhang, W. Lv, Y. Tao, Q.-H. Yang, *Energy Environ. Sci.* **2015**, 8, 1390.
- [17] O. L. Blakslee, D. G. Proctor, E. J. Seldin, G. B. Spence, T. Weng, *J. Appl. Phys.* **1970**, 41, 3373.
- [18] A. Cosculluela, J. Farre, *J. Phys. Iv* **1997**, 07, C3.
- [19] T. Zhu, J. Li, *Prog. Mater. Sci.* **2010**, 55, 710.
- [20] a) L. J. Gibson, M. F. Ashby, *Cellular solids structure and properties*, **1997**; b) M. F. Ashby, R. F. M. Medalist, *Metall. Trans. A* **1983**, 14, 1755.
- [21] H. O. Pierson, *Handbook of carbon, graphite, diamond and fullerenes - properties, processing and applications*, **1993**.
- [22] H. I. Rasool, C. Ophus, W. S. Klug, A. Zettl, J. K. Gimzewski, *Nat. Commun.* **2013**, 4, 2811.
- [23] C. Cao, M. Daly, C. V. Singh, Y. Sun, T. Filleter, *Carbon* **2015**, 81, 497.
- [24] Y. Bai, R. Zhang, X. Ye, Z. Zhu, H. Xie, B. Shen, D. Cai, B. Liu, C. Zhang, Z. Jia, S. Zhang, X. Li, F. Wei, *Nat. Nanotech.* **2018**, 13, 589.
- [25] J. Biener, S. Dasgupta, L. Shao, D. Wang, M. A. Worsley, A. Wittstock, J. R. I. Lee, M. M. Biener, C. A. Orme, S. O. Kucheyev, B. C. Wood, T. M. Willey, A. V. Hamza, J. Weissmüller, H. Hahn, T. F. Baumann, *Adv. Mater.* **2012**, 24, 5083.
- [26] Z. Q. Liu, W. H. Wang, M. Q. Jiang, Z. F. Zhang, *Phil. Mag. Lett.* **2014**, 94, 658.
- [27] a) M. D. Uchic, D. M. Dimiduk, J. N. Florando, W. D. Nix, *Science* **2004**, 305, 986; b) J. R. Greer, J. T. M. De Hosson, *Prog. Mater. Sci.* **2011**, 56, 654.
- [28] a) Z. W. Shan, J. Li, Y. Q. Cheng, A. M. Minor, S. A. Syed Asif, O. L. Warren, E. Ma, *Phys. Rev. B* **2008**, 77, 155419; b) C. A. Volkert, A. Donohue, F. Spaepen, *J. Appl. Phys.* **2008**, 103, 083539; c) H. Guo, P. F. Yan, Y. B. Wang, J. Tan, Z. F. Zhang, M. L. Sui, E. Ma, *Nat. Mater.* **2007**, 6, 735; d) D. Jang, J. R. Greer, *Nat. Mater.* **2010**, 9, 215.
- [29] a) F. Östlund, P. R. Howie, R. Ghisleni, S. Korte, K. Leifer, W. J. Clegg, J. Michler, *Philos. Mag.* **2010**, 91, 1190; b) F. Östlund, K. Rzepiejewska-Malyska, K. Leifer, L. M. Hale, Y. Tang, R. Ballarini, W. W. Gerberich, J. Michler, *Adv. Funct. Mater.* **2009**, 19, 2439; c) P. R. Howie, S. Korte, W. J. Clegg, *J. Mater. Res.* **2012**, 27, 141.
- [30] J. Bauer, S. Hengsbach, I. Tesari, R. Schwaiger, O. Kraft, *Proc. Natl. Acad. Sci. USA* **2014**, 111, 2453.
- [31] J. Schwiedrzik, R. Raghavan, A. Bürki, V. LeNader, U. Wolfram, J. Michler, P. Zysset, *Nat. Mater.* **2014**, 13, 740.
- [32] W. C. Oliver, G. M. Pharr, *J. Mater. Res.* **1992**, 7, 1564.
- [33] H. Fei, A. Abraham, N. Chawla, H. Jiang, *J. Appl. Mech.* **2012**, 79, 061011.
- [34] S. Plimpton, *J. Comput. Phys.* **1995**, 117, 1.
- [35] S. J. Stuart, A. B. Tutein, J. A. Harrison, *J. Chem. Phys.* **2000**, 112, 6472.
- [36] J. Li, *Model. Simul. Mater. Sc* **2003**, 11, 173.

**The table of contents entry**

Keywords: Graphene, three-dimensional assembly, mechanical properties, size effects, in situ electron microscopy, nanoindentation

Dai-Ming Tang, Cui-Lan Ren, Ling Zhang\*, Ying Tao, Peng Zhang, Wei Lv, Xiang-Ling Jia, Xiaojuan Jiang, Guangmin Zhou, Takahito Ohmura, Ping Huai, Feng Li, Yoshio Bando, Dmitri Golberg\*, Quan-Hong Yang\*

**Size effects on the mechanical properties of nanoporous graphene networks**

Size scaling effects on the mechanical properties of graphene-assembled networks are investigated by in situ pillar compression inside electron microscopes and molecular dynamics simulations. As the diameters reduce to  $\sim 100$  nm, the strength is drastically enhanced to  $> 1$  GPa. A brittle-to-ductile transition is revealed and understood by the competition between volumetric deformation energy and critical dilation energy.